

Disclinations provide the missing mechanism for deforming olivine-rich rocks in the mantle

Patrick Cordier¹, Sylvie Demouchy², Benoît Beausir³, Vincent Taupin³, Fabrice Barou² & Claude Fressengeas³

Mantle flow involves large strains of polymineral aggregates. The strongly anisotropic plastic response of each individual grain in the aggregate results from the interactions between neighbouring grains and the continuity of material displacement across the grain boundaries. Orthorhombic olivine, which is the dominant mineral phase of the Earth's upper mantle, does not exhibit enough slip systems to accommodate a general deformation state by intracrystalline slip without inducing damage. Here we show that a more general description of the deformation process that includes the motion of rotational defects referred to as disclinations can solve the olivine deformation paradox. We use high-resolution electron backscattering diffraction (EBSD) maps of deformed olivine aggregates to resolve the disclinations. The disclinations are found to decorate grain boundaries in olivine samples deformed experimentally and in nature. We present a disclination-based model of a high-angle tilt boundary in olivine, which demonstrates that an applied shear induces grain-boundary migration through disclination motion. This new approach clarifies grain-boundary-mediated plasticity in polycrystalline aggregates. By providing the missing mechanism for describing plastic flow in olivine, this work will permit multiscale modelling of the rheology of the upper mantle, from the atomic scale to the scale of the flow.

There is a large body of work describing plastic deformation of olivine^{1,2}, which is by far the most abundant (~60–70%) and the weakest upper-mantle mineral under a wide range of thermo-mechanical conditions. In this literature, the prevailing deformation mechanisms include the transport of matter by diffusion and of shear by motion of dislocations. However, the dislocation-based crystal plasticity of olivine is challenged by a lack of slip systems. For plastic flow to occur homogeneously by dislocation glide alone, at least five independent slip systems must operate, according to the Von Mises criterion³. This requirement can be relaxed to four slip systems if inhomogeneous flow is allowed⁴. In orthorhombic olivine (space group *Pbnm*), plastic slip is restricted to [100] and [001] directions with no possibility of shear along [010]. Hence, only four slip systems are available: [100](010), [100](001), [001](010) and [001](100). In this case, the only non-vanishing components of the corresponding Schmid tensors (the number of overbars indicates the rank of the tensor) \bar{m} are: $m_{12}^{[100](010)} = m_{21}^{[100](010)} = 0.5$; $m_{13}^{[100](001)} = m_{31}^{[100](001)} = 0.5$; $m_{23}^{[001](010)} = m_{32}^{[001](010)} = 0.5$; and $m_{13}^{[001](100)} = m_{31}^{[001](100)} = 0.5$. Thus, the slip systems [100](001) and [001](100) are not linearly independent, and only the three-system sets ([100](010), [100](001) and [001](010)) and ([100](010), [001](010) and [001](100)) are. Therefore, olivine aggregates do not fulfil Hutchinson's relaxed condition, and arbitrary deformation can only be accommodated if additional degrees of freedom are provided, by climb (that is, dislocation motion out of the glide plane by absorption/emission of point defects) for instance. However, if climb is able to help dislocations to overcome obstacles, the climb rate is not efficient enough in olivine to provide a significant contribution to the strain (see Supplementary Information). Hirth and Kohlstedt⁵ have proposed that grain-boundary sliding accommodated by (that is, rate limited by) dislocation motion could provide an alternative mechanism and account for a creep regime

observed for olivine in which strain rate is nonlinear in stress and sensitive to grain size⁶. However, grain-boundary sliding requires displacement discontinuity⁷ and/or rotational discontinuity at grain boundaries, which is likely to induce damage. More recently, Detrez *et al.*⁸ have explored theoretically the possibility that the lack of slip systems

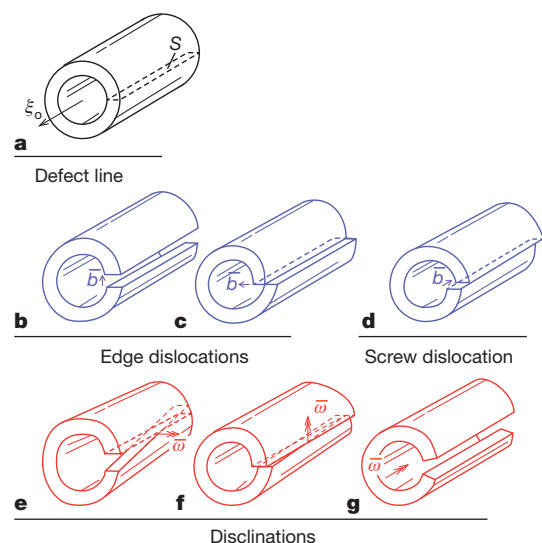


Figure 1 | Volterra's distortions. **a**, Reference cylinder with defect line ξ_0 and cut surface S . **b, c**, Edge dislocations with Burgers vector b . **d**, Screw dislocation with Burgers vector b . **e, f**, Twist disclinations with Frank vector $\bar{\omega}$. **g**, Wedge disclination with Frank vector $\bar{\omega}$.

¹Unité Matériaux et Transformations, UMR 8207 CNRS and Université Lille 1, 59650 Villeneuve d'Ascq, France. ²Geosciences Montpellier, UMR 5342 CNRS and Université de Montpellier 2, 34095 Montpellier, France. ³Laboratoire d'Etude des Microstructures et de Mécanique des Matériaux, UMR 7239 CNRS and Université de Lorraine, Ile du Saulcy, 57045 Metz Cedex, France.

Table 1 | The compatible and incompatible elasto-static defect theory

| | Translational | | Rotational |
|------------------------------------|--|---|---|
| Displacement vector | \bar{u} | Rotation vector | $\bar{\omega} = \frac{1}{2} \text{curl } \bar{u}$ |
| Strain tensor | $\bar{\varepsilon} = \frac{1}{2} (\text{grad } \bar{u} + \text{grad}^t \bar{u})$ | Curvature tensor | $\bar{\kappa} = \text{grad } \bar{\omega}$ |
| Cauchy stress tensor | $\bar{\sigma} = \bar{C} : \bar{\varepsilon}^e$ | Couple-stress tensor | $\bar{M} = \bar{A} : \bar{\kappa}^e$ |
| Equilibrium condition for stresses | $\text{div } \bar{\sigma} = 0$ | Equilibrium condition for couple stresses | $\text{div } \bar{M} = 0$ |
| Nye's dislocation density tensor | $\bar{\alpha} = \text{curl } \bar{U}_e = -\text{curl } \bar{U}_p$ | Disclination density tensor | $\bar{\theta} = \text{curl } \bar{\kappa}_e = -\text{curl } \bar{\kappa}_p$ |

The left column displays the features of translational elasticity and plasticity; the right column shows the rotational counterparts. The derivation of these elements is provided in the Supplementary Information.

in olivine could be overcome by purely diffusive (that is, linear) mechanisms operating at grain boundaries. They showed, however, that such a mechanism was unable to sustain a nonlinear rheology.

Disclinations in solids

Here we show that the lack of slip systems in olivine can be offset by a more general analysis of plastic deformation in solids. Indeed, plastic deformation does not result only from the motion of dislocations. Dislocations are the crystal defects arising from translational lattice incompatibility, as measured by the Burgers vector or Nye's dislocation density

tensor $\bar{\alpha}$ (see Supplementary Information for a summary of the elasto-plastic field theory of crystal defects). Similarly, the rotational incompatibility of the crystal lattice can be related to defects called disclinations. Dislocations and disclinations were both proposed by Volterra⁹ to account for the discontinuity of elastic displacements and rotations along surfaces in a solid containing defects (Fig. 1). In the thought experiment proposed by Volterra, a cut is made in a defect-containing elastic cylinder, from which the core of the line defect, lying along the cylinder axis, has been removed. In the presence of lattice incompatibility, the cut induces rigid-body motion of one edge of the cut with

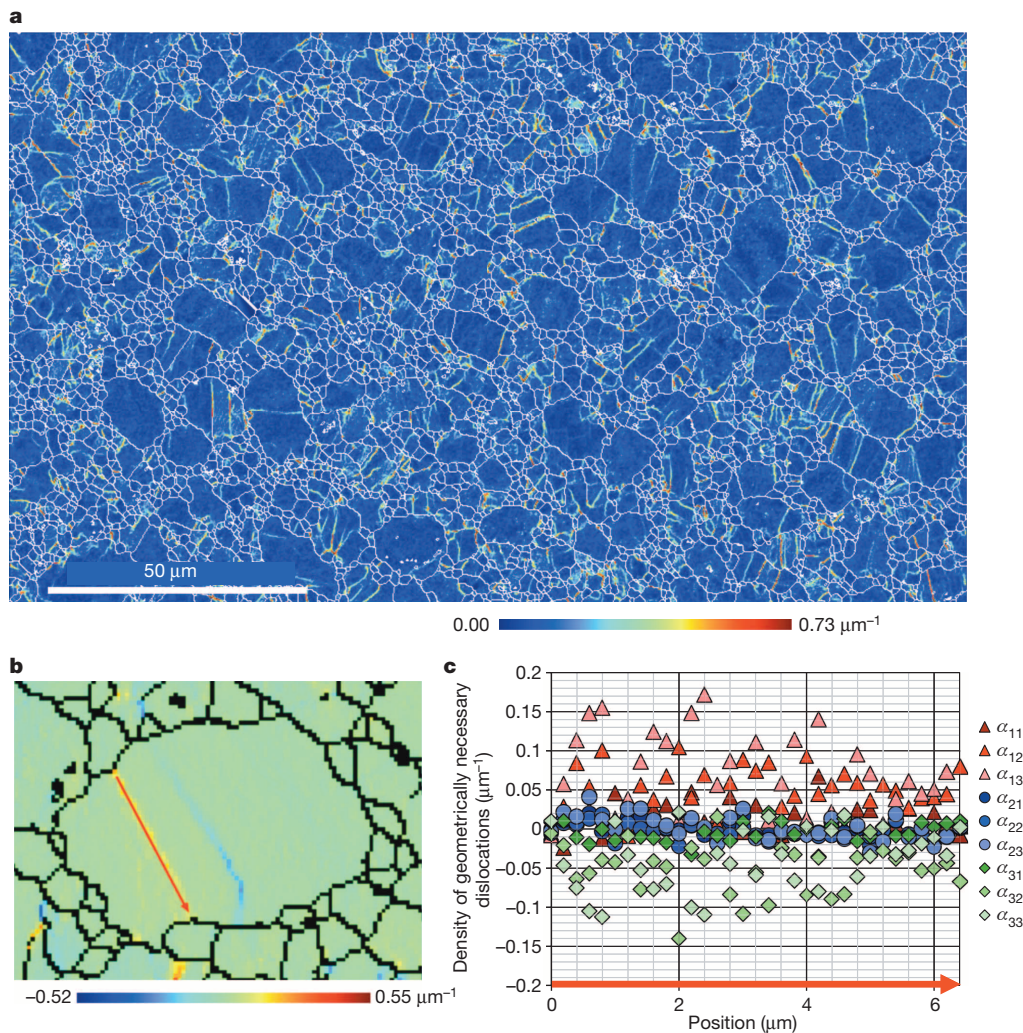


Figure 2 | Geometrically necessary dislocation densities in olivine. Densities are given per micrometre. **a**, Entrywise norm of Nye tensor $\bar{\alpha}$ in sample PoEM22 (experimentally deformed at 8% in compression at 900 °C). **b**, Close-up, showing the α_{13} component with an opposite curvature on the subgrain boundary. **c**, Nye tensor components projected in the crystal reference system

along a subgrain boundary (red arrow); the [100]-glide, [010]-glide and [001]-glide are plotted with red, blue and green marks, respectively. With [100] and [001] edge dislocations prevailing, the subgrain boundary is essentially a tilt boundary. We note the occasional presence of a twist component through sets of screw dislocations at a right angle (α_{11}, α_{33}).

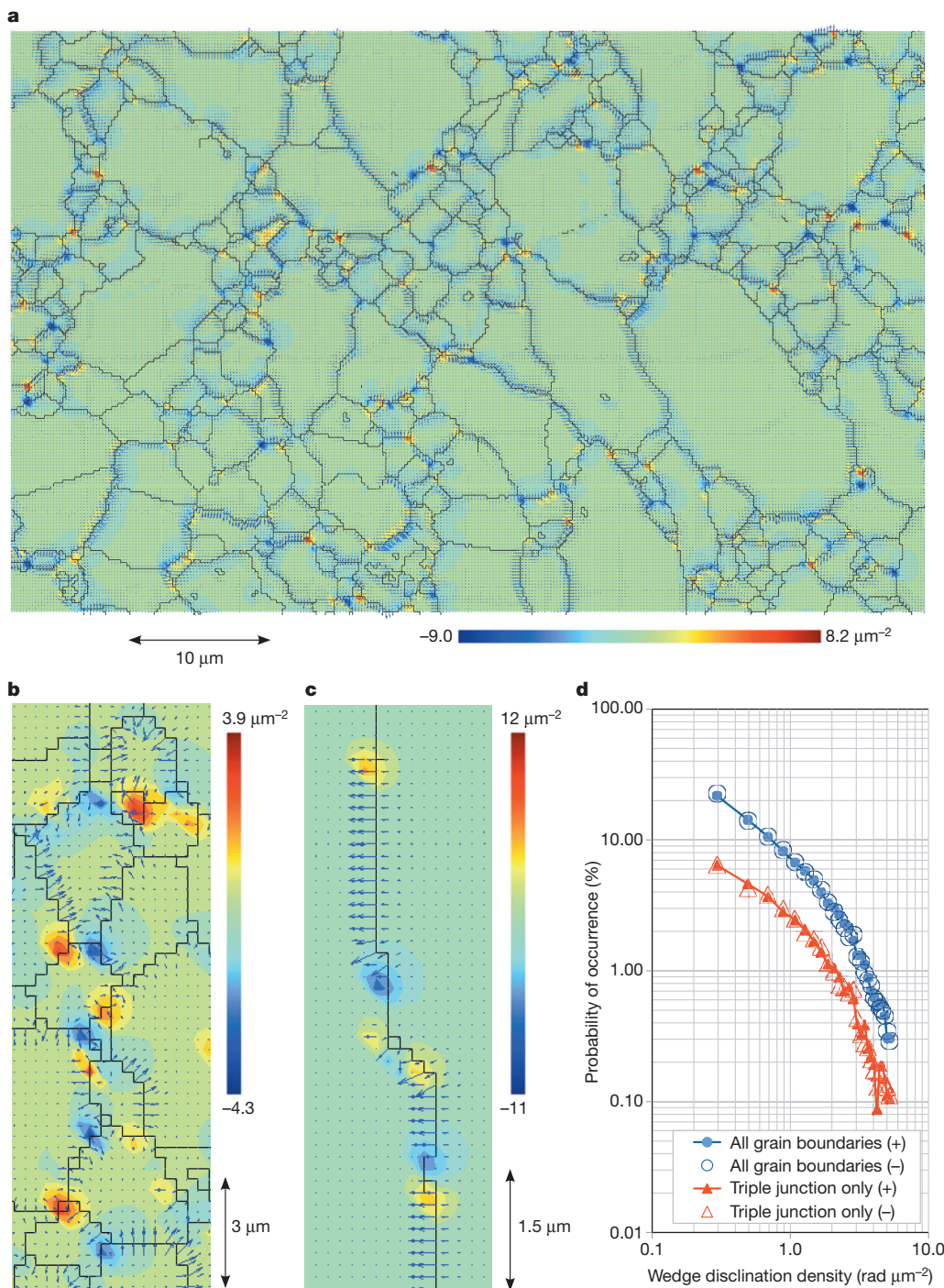


Figure 3 | Three maps representing the density of wedge disclinations θ_{33} in three deformed olivine aggregates, and the probability of occurrence for sample T0548. The density is given in radians per square micrometre. (See below and Supplementary Information for a detailed description of the samples.) The local Burgers vectors arising from edge dislocations are represented by the blue arrows: their horizontal and vertical components are respectively α_{13} and α_{23} (given per micrometre). **a**, Sample PoEM22 (experimentally deformed 8% compression at 900 °C). This low-magnification

map shows the pervasive occurrence of disclinations in grain boundaries.

b, Sample T0548 (experimentally deformed 250% torsion at 1,200 °C).

c, Sample OOM, a naturally deformed mylonitic harzburgite from the Oman ophiolite (Sumail massif). **d**, Probability of occurrence of positive (+) versus negative (-) wedge disclination density θ_{33} in sample T0548. Filled circles indicate all positive wedges, open circles indicate all negative wedges, filled triangles indicate positive triple junction wedges and open triangles indicate negative triple junction wedges.

respect to the other. When this motion is a translation, the defect is referred to as a dislocation, whose strength is the so-called Burgers vector, that is, the (space-independent) translation vector. A disclination is obtained when the motion is a pure rotation. The strength of the disclination is the relative rotation vector of the undeformed edges of the cut, referred to as the Frank vector. The relative displacement of the

edges in this rotation also gives rise to a space-dependent Burgers vector associated with the disclination. As rotational defects, disclinations are set into motion by moments of stresses. This motion results in disclination-mediated plasticity not accounted for by the dislocation theory. Disclinations have long been neglected in the field theory of crystal defects, including for deep Earth minerals, owing to the very large level of elastic

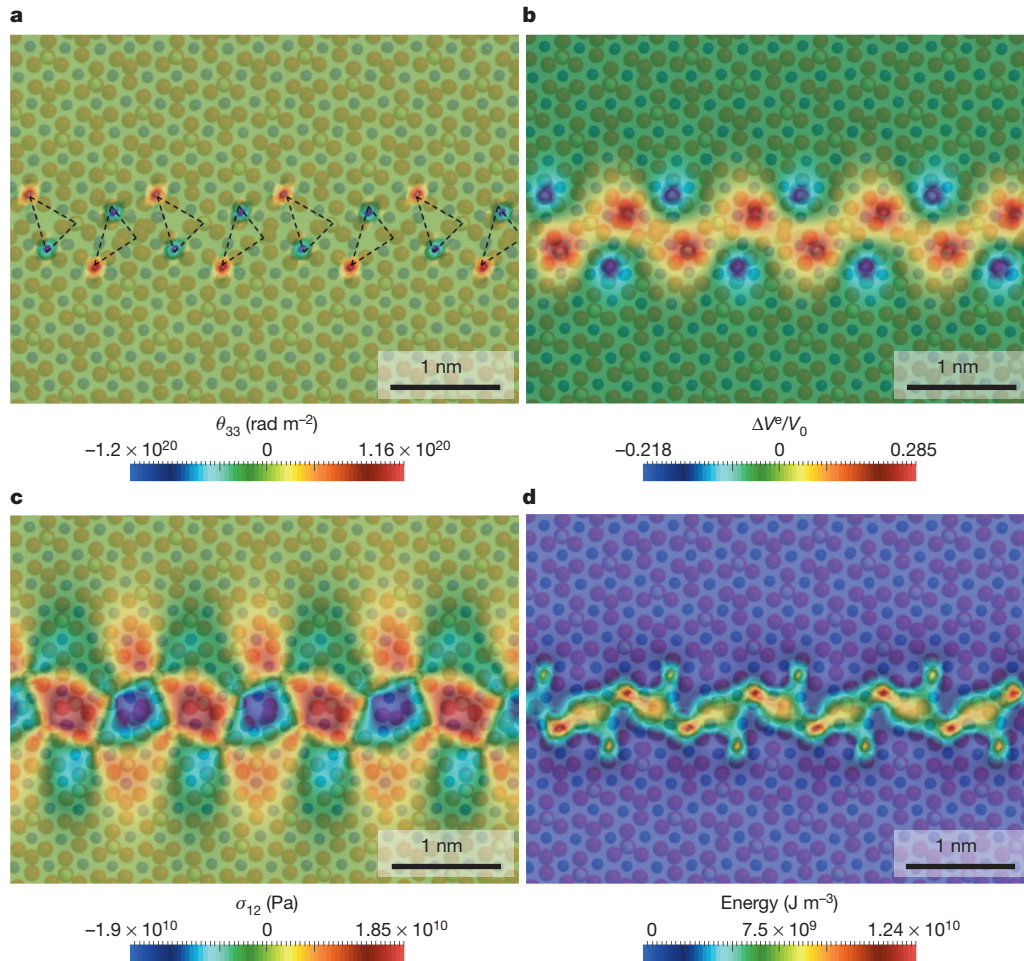


Figure 4 | Disclination-based modelling of the (011)/[100] tilt grain boundary with misorientation 60° modelled at the atomic scale in olivine²¹. **a**, Initial wedge disclination density θ_{33} (given in radians per square metre) used in the simulations. The triangles represent the structural units

energy they involve, compared with dislocations, which precludes their occurrence as isolated crystalline objects¹⁰. However, self-screened configurations, such as disclination dipoles, involve relatively small elastic energy levels^{11,12}. It was recently shown that disclination dipoles are pervasive along boundaries and subgrain boundaries in severely deformed copper, inclusion-free steel, electrodeposited aluminium thin film and in recrystallized titanium¹³, highlighting the importance of rotational defects in metallic polycrystals.

Disclinations evidenced by EBSD

To check whether, like metals, deformed olivines contain disclinations, we used EBSD, which is a technique well adapted to local lattice orientation measurements. From the orientation differences $\Delta\theta_i$ between neighbouring points separated by Δx_j the elastic curvature tensor (see Table 1) can be captured:

$$\kappa_{ij}^e = \frac{\partial\theta_i}{\partial x_j} \approx \frac{\Delta\theta_i}{\Delta x_j} \quad (1)$$

In fact, only six components of the elastic curvature tensor can be determined, because differences along the direction perpendicular to the surface are not available¹⁴ (see Methods). The Nye's dislocation density tensor can then be approximately derived as

$$\alpha_{ik} = \delta_{ik}\kappa_{mm}^e - \kappa_{ki}^e \quad (2)$$

Using this equation and considering the constraints on the measurements, five dislocation densities can be recovered in the reference frame

proposed by ref. 21 (see Methods for the construction of this model). **b**, Elastic dilations and contractions. **c**, Shear stress σ_{12} (given in pascals). **d**, Elastic energy density (given in joules per cubic metre).

of the laboratory, namely α_{12} , α_{13} , α_{21} , α_{23} and α_{33} , if the surface lies along the (1, 2) directions. Knowing the crystal orientation at each measurement point, these dislocation densities can be rotated in the crystallographic reference frame (they are then referred to as α_{ij}^c , where 'c' indicates 'crystallographic'). Figure 2a, b shows a scalar dislocation measure (that is, the length of the local Burgers vector per unit surface resulting from the edge dislocation densities α_{13} , α_{23}) in olivine polycrystals deformed experimentally^{15,16}. One of the most remarkable features of these maps is the occurrence of numerous straight subgrain boundaries, especially in the larger grains. These subgrain boundaries are commonly observed in olivine grains^{17–19} in naturally deformed mantle rocks. Made of geometrically necessary dislocations²⁰, subgrain boundaries accommodate intracrystalline misorientations and represent a first indication (largely overlooked) of the importance of these components in the plastic deformation of olivine. The analysis of the α_{ij}^c components allows us to characterize the dislocation types present in the sample. Figure 2c shows such an analysis performed along one of the subgrain boundaries (Fig. 2b). The boundary is made of [100] dislocations ($\alpha_{11}^c, \alpha_{12}^c, \alpha_{13}^c$) described in the crystal reference frame and of [001] dislocations ($\alpha_{31}^c, \alpha_{32}^c, \alpha_{33}^c$). The components corresponding to [010]-glide ($\alpha_{21}^c, \alpha_{22}^c, \alpha_{23}^c$) are negligible, in agreement with the known characteristics of olivine. Further characterization within the samples considered in this study leads to the same conclusion and demonstrates that our analysis allows the dislocation content in deformed olivine to be resolved. Previously, only decoration (annealing followed by optical microscopy or scanning electron microscopy) or transmission electron microscopy

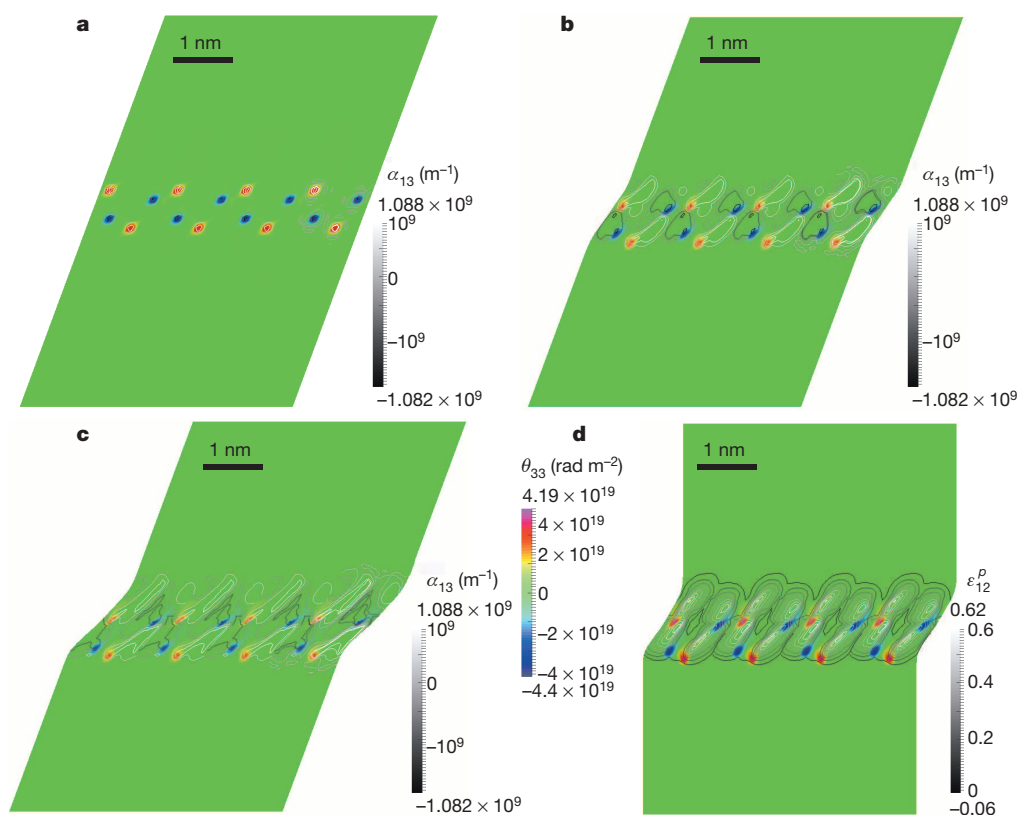


Figure 5 | Shear-coupled boundary migration of the (011)/[100] tilt grain boundary of Fig. 4. The wedge disclination density θ_{33} (in radians per square metre) is colour-coded. A to C shows the downward migration of the disclinations from 0 ms to 170 ms, when a positive shear strain of 0.2 is applied. Black and white contours show the edge dislocation density α_{13} (per metre). D shows the unloaded bicrystal after 170 ms, revealing shear-coupled migration. Black and white contours show the positive plastic shear strain ε_{12}^p produced by the downward migration of the grain boundary. For this particular misorientation, the shear coupling factor $\beta = -0.8$ resulting from a downward migration coupled with positive shear is negative, but it may be positive for different misorientations.

were available to characterize dislocation microstructures in olivine. This new technique also has another use, in that the variations in space of the elastic curvatures tensor yield the disclination densities:

$$\theta_{ij} = e_{jkl} \kappa_{il,k}^e \quad (3)$$

Figure 3 presents the results of this analysis performed on the experimentally and naturally deformed samples. It shows that the grain boundaries are associated with dislocation densities but also that they contain numerous disclinations correlating with the variations in misorientation along the grain boundary. Disclinations are also frequently associated with triple junctions. A visual inspection suggests that positive and negative disclinations are spatially coupled in the form of dipoles. The statistical analysis of Fig. 3d demonstrates that positive and negative wedge disclination densities balance perfectly, not only for the set of all grain boundaries but also for the subset composed of triple junctions. The present study shows that disclination dipoles and the rotational incompatibility they reveal represent a significant component of the deformation field in plastically deformed olivines, which is localized in grain boundaries and complements the known contribution of dislocations.

Disclinations-based grain-boundary migration

To illustrate the role of disclinations on plasticity, we built a model of a tilt boundary in olivine with a periodic wedge disclination array. We started from the (011)/[100] tilt grain boundary with misorientation 60° already modelled at the atomic scale in olivine²¹. Figure 4 shows the disclination model built on this boundary. The wedge disclination density spots are located on the vertices of the structural units²¹. The zigzag arrangements of the wedge disclinations result in a very efficient self-screening quasi-quadrupole configuration¹¹. Indeed, most of the energy is located within the structural units identified on the atomistic model. Our disclination-based model leads to a grain-boundary energy of 1.3 J m^{-2} , in excellent agreement with the value proposed by Adjaoud *et al.*²¹ based on atomistic calculations of 1.28 J m^{-2} . When a shear stress is applied to this disclination distribution, the strong variations of the local shear strain within the defect-containing areas generate couple stresses. In response to this couple-stress field, the disclination

dipoles are set into motion normal to the boundary (Fig. 5), producing plastic shear parallel to the boundary. The disclination dipole structure is maintained during this motion, which induces both migration of the boundary and shear of the crystal. Like other grain-boundary deformation mechanisms, grain-boundary migration/disclination motion is dependent on grain size. It is more apparent when the proportion of matter involved in grain boundaries is higher, that is, at small grain sizes.

We note that this disclination-induced grain-boundary migration mechanism can exhibit linearity, or nonlinearity in stress, depending on the assumed relationship between disclination velocity and the associated driving force. A more comprehensive study of the disclination structure, energy and mobility of grain boundaries as functions of misorientations is clearly needed to reach an eventual description of the rheology of an olivine aggregate. EBSD-based disclination imaging in naturally deformed olivine aggregates will allow these models to be established. Our model might also explain the formation of crystal-preferred orientations in materials deformed in the Newtonian creep regime²², as recently documented for olivine²³.

METHODS SUMMARY

We used high-resolution EBSD to analyse the microstructure of four aggregates. These were a mylonitic harzburgite (OOM) from the Oman ophiolite (Sumail massif) and three olivine aggregates: a hot-pressed undeformed sample (PI-1619; ref. 15), a deformed sample in compression at 300 MPa and 900°C (PoEM22) and a deformed sample under torsion at 300 MPa and $1,200^\circ \text{C}$ (T0548). EBSD analyses were conducted with a CamScan X500FE CrystalProbe. The operating conditions were 15 kV and 2.5-nA current under low-vacuum conditions (4–5 Pa of gaseous nitrogen) with a 20-mm working distance. The step size was $0.15 \mu\text{m}$ or $0.2 \mu\text{m}$. The data were acquired and treated with CHANNEL5 software (http://caf.ua.edu/wp-content/uploads/docs/JEOL-7000F-Oxford_Channel_5_User_Manual.pdf).

The elastic curvature tensor $\overline{\kappa}_c^e$ (where 'e' indicates 'elastic') was recovered from the EBSD orientation maps. By additionally recovering the elastic strain field $\overline{\varepsilon}_c$ and building the curl of this field $\overline{\text{curl}} \overline{\varepsilon}_c$, the dislocation density tensor $\overline{\alpha}$ can be inferred exactly. In this work, as in most studies, the $\overline{\text{curl}} \overline{\varepsilon}_c$ term is overlooked, and $\overline{\alpha}$ is approximated by

$$\overline{\alpha} = \text{Tr}(\overline{\kappa}_c^e) \overline{\mathbb{I}} - \overline{\kappa}_c^t \quad (4)$$

In addition, the disclination density tensor $\bar{\bar{\theta}}$ may be recovered by building the curl of $\bar{\bar{\kappa}}_c$. When a single planar orientation map is known, only five components of $\bar{\bar{\kappa}}$ and three components of $\bar{\bar{\theta}}$ can be determined. If the planar directions are labelled (1, 2) in the sample frame, the available components are $(\alpha_{12}, \alpha_{13}, \alpha_{21}, \alpha_{23}, \alpha_{33})$ and $(\theta_{13}, \theta_{23}, \theta_{33})$. To predict the grain-boundary structure and mobility, we used a theory of crystal defect fields (disclinations and dislocations) defined at the interatomic scale^{24,25}. Our modelling paradigm is to account for the lattice incompatibility arising from crystal defects by focusing on the defect densities, rather than on the atoms themselves. The theory has the standard mathematical structure of a set of partial differential equations with boundary conditions. The unknown fields are the tensorial defect densities (dislocations and disclinations) and displacement vector fields, with standard boundary conditions on displacements and traction/moment vectors. As a consequence of this boundary value structure, approximate solutions can be generated by using finite-element methods²⁶.

Online Content Any additional Methods, Extended Data display items and Source Data are available in the online version of the paper; references unique to these sections appear only in the online paper.

Received 9 July 2013; accepted 14 January 2014.

Published online 26 February 2014.

- Kohlstedt, D. L., Evans, B. & Mackwell, S. J. Strength of the lithosphere—constraints imposed by laboratory experiments. *J. Geophys. Res.* **100** (B9), 17587–17602 (1995).
- Hirth, G. & Kohlstedt, D. L. in *Inside the Subduction Factory* (ed. Eiler, J.) 83–105 (American Geophysical Union, 2003).
- Von Mises, R. Mechanik der plastischen Formänderung von Kristallen. *Z. Angew. Math. Mech.* **8**, 161–185 (1928).
- Hutchinson, J. W. Creep and plasticity of hexagonal polycrystals as related to single crystal slip. *Metall. Trans. A* **8**, 1465–1469 (1977).
- Hirth, G. & Kohlstedt, D. L. Experimental constraints on the dynamics of the partially molten upper-mantle. 2. Deformation in the dislocation creep regime. *J. Geophys. Res.* **100** (B8), 15441–15449 (1995).
- Hansen, L. N., Zimmerman, M. E. & Kohlstedt, D. L. Grain boundary sliding in San Carlos olivine: flow law parameters and crystallographic-preferred orientation. *J. Geophys. Res.* **116**, B08201 (2011).
- Langdon, T. G. Grain boundary sliding revisited: developments in sliding over four decades. *J. Mater. Sci.* **41**, 597–609 (2006).
- Detrez, F., Castelnaud, O., Cordier, P., Merkel, S. & Raterron, P. Second-order theory for the effective behavior in viscoplastic polycrystals without sufficient slip system families: application to olivine. *J. Mech. Phys. Solids* (submitted).
- Volterra, V. Sur l'équilibre des corps élastiques multiplement connexes. *Ann. Sci. Ecole Norm. Supér.* **24**, 401–517 (1907).
- Friedel, J. *Dislocations* (Pergamon, 1967).
- Romanov, A. E. & Vladimirov, V. I. in *Dislocations in Solids* Vol. 9 (ed. Nabarro, F. R. N.) 191–402 (North-Holland, 1992).
- Romanov, A. E. & Kolesnikova, A. L. Application of disclination concept to solid structures. *Prog. Mater. Sci.* **54**, 740–769 (2009).
- Beausir, B. & Fressengeas, C. Disclination densities from EBSD orientation mapping. *Int. J. Solids Struct.* **50**, 137–146 (2013).
- Pantleon, W. Resolving the geometrically necessary dislocation content by conventional electron backscattering diffraction. *Scr. Mater.* **58**, 994–997 (2008).
- Demouchy, S., Tommasi, A., Barou, F., Mainprice, D. & Cordier, P. Deformation of olivine in torsion under hydrous conditions. *Phys. Earth Planet. Inter.* **202**, 56–70 (2012).
- Seront, B. *Déformation Expérimentale à Haute Pression et Haute Température d'Agrégats Polycristallins de Plagioclase et d'Olivine*. PhD thesis, Montpellier Univ. (1993).
- Arndt, N. T. et al. Olivine, and the origin of kimberlite. *J. Petrol.* **51**, 573–602 (2010).
- Soustelle, V., Tommasi, A., Demouchy, S. & Ionov, D. A. Deformation and fluid-rock interaction in the supra-subduction mantle: microstructures and water contents in peridotite xenoliths from the Avacha Volcano, Kamchatka. *J. Petrol.* **51**, 363–394 (2010).
- Falus, G., Tommasi, A. & Soustelle, V. The effect of dynamic recrystallization on olivine crystal preferred orientations in mantle xenoliths deformed under varied stress conditions. *J. Struct. Geol.* **33**, 1528–1540 (2011).
- Ashby, M. F. Deformation of plastically non-homogeneous materials. *Phil. Mag.* **21**, 399–424 (1970).
- Adjaoud, O., Marquardt, K. & Jahn, S. Atomic structures and energies of grain boundaries in Mg₂SiO₄ forsterite from atomistic modeling. *Phys. Chem. Miner.* **39**, 749–760 (2012).
- Gomez Barreiro, J. et al. Preferred orientation of anorthite deformed experimentally in Newtonian creep. *Earth Planet. Sci. Lett.* **264**, 188–207 (2007).
- Miyazaki, T., Sueyoshi, K. & Hiraga, T. Olivine crystals align during diffusion creep of Earth's upper mantle. *Nature* **502**, 321–326 (2013).
- Fressengeas, C., Taupin, V. & Capolungo, L. An elasto-plastic theory of dislocation and disclination fields. *Int. J. Solids Struct.* **48**, 3499–3509 (2011).
- Taupin, V., Capolungo, L., Fressengeas, C., Das, A. & Upadhyay, M. Grain boundary modeling using an elasto-plastic theory of dislocation and disclination fields. *J. Mech. Phys. Solids* **61**, 370–384 (2013).
- Varadhan, S. N., Beaudoin, A. J., Acharya, A. & Fressengeas, C. Dislocation transport using an explicit Galerkin/least-squares formulation. *Model. Simul. Mater. Sci. Eng.* **14**, 1245–1270 (2006).

Supplementary Information is available in the online version of the paper.

Acknowledgements We acknowledge financial support from the European Research Council under the Seventh Framework Programme (FP7—ERC grant number 290424—RheoMan), from a Marie Curie fellowship (FP7-PEOPLE-20074-3-IRG, grant number 230748-PoEM) and from the Agence Nationale de la Recherche (grant number ANR-11-JS09-007-01, NanoMec).

Author Contributions S.D. deformed the olivine samples and performed the EBSD measurements (with the help of F.B.). B.B., V.T. and C.F. performed the data analysis and disclination modelling. P.C. wrote the paper with feedback and contributions from all co-authors. All authors discussed and interpreted the results.

Author Information Reprints and permissions information is available at www.nature.com/reprints. The authors declare no competing financial interests. Readers are welcome to comment on the online version of the paper. Correspondence and requests for materials should be addressed to P.C. (patrick.cordier@univ-lille1.fr).

METHODS

This section describes the methods we used to analyse the defects (dislocations and disclinations) from naturally and experimentally deformed olivine samples as well as the disclination-based model for shear grain-boundary migration. It is largely based on the elasto-plastic field theory of crystal defects described in several references cited in the text. Readers unfamiliar with this field may first read the introduction to the Supplementary Information.

Dislocation and disclination analysis from EBSD orientation mapping. A mylonitic harzburgite (sample OOM) from the Oman ophiolite (Sumail massif) was selected as representative of a highly deformed uppermost mantle. Modal compositions are: 82% olivine, 15% enstatite, 1.5% diopside, and 1% spinel with minor traces of chlorite and amphibole. The specimen is fine-grained (average grain size of 90 μm), but with three generations of grains¹⁶: recrystallized equigranular grains (120–150 μm), a few larger grains (800–1,000 μm) and largely distributed bands of ultra-mylonitic olivine (<50 μm , which are the sections analysed here).

Experimentally deformed olivine sample PoEM22. Hot-pressing and deformation experiments were carried out at a confining pressure of 300 MPa in a high-resolution gas-medium mechanical testing apparatus (Paterson apparatus) at Geosciences Montpellier (France). A dry fine-grained powder of olivine (average grain size of 7 μm ; ref. 27) was cold-pressed into a thin Ni sleeve (200 μm thick) with an outer diameter of 9.90 mm and 20 mm in height. Both ends were closed with a thin fitted Ni disk (200 μm thick) held in place by an external thin rim of superglue. The Ni sleeve was used to buffer oxygen fugacity (along the Ni–NiO curve). The sample assembly for all types of deformation experiment was then encapsulated along with zirconia and alumina pistons and spacers inside an iron jacket²⁷. The aggregate was hot-pressed at 1,250 °C under a confining pressure of 300 MPa for 3 h; then the temperature was slowly decreased down to 900 °C. In parallel, the confining pressure was carefully kept at 300 MPa during the temperature decrease. Tri-axial deformation at constant displacement rate was initiated one hour after temperature stabilization at 900 °C for sample PoEM22 (each run produced one sample) (ref. 28). The strain rate was $1.1 \times 10^{-5} \text{ s}^{-1}$. A maximal strain of 7.6 was reached. The stress–strain curves show strong work-hardening.

Experimentally deformed olivine sample T0548. Hot-pressing experiments were carried out at a confining pressure of 300 MPa in a high-resolution gas-medium mechanical testing apparatus (Paterson apparatus) at the Department of Geology and Geophysics, University of Minnesota, USA. A dry fine-grained powder of olivine (average grain size 3.8 μm) was cold-pressed into a thin Ni canister at 1,250 °C for 3 h under hydrostatic pressure¹⁵. After sample recovery and further preparation, the olivine dense aggregates were transferred to a high-resolution gas-medium torsion apparatus²⁹ for deformation in torsion at the Department of Geology and Geophysics, University of Minnesota, USA. Deformation at constant rotation rate¹⁵ was started after one hour after annealing at temperature 1,200 °C and 300 MPa of confining pressure with a force of 1 kN (16 MPa) applied on the sample. The shear strain rate was $8.0 \times 10^{-5} \text{ s}^{-1}$ (equivalent to a strain rate of $4.6 \times 10^{-5} \text{ s}^{-1}$). A maximal shear stress of 158 MPa (equivalent to a axial stress of 248 MPa) was reached. The finite shear strain was 3.04.

Experimentally sintered and undeformed olivine sample PI-1619. The hot-pressing experiment was carried out at a confining pressure of 300 MPa in a high-resolution gas-medium mechanical testing apparatus (Paterson apparatus) at the University of Minnesota, USA. A dry fine-grained powder of olivine was first cold-pressed at 100 MPa into a thick-walled Ni canister¹⁵ (26 mm long, 11.7 mm outside diameter, 10 mm inside diameter). Afterwards, both ends were closed with a fitted Ni plug. The Ni sleeve was used to buffer oxygen fugacity (along the Ni–NiO curve) as for the deformed olivine aggregate. Water was added to the canister, but did not affect the hot-pressing step. The sample assembly for all types of hot-pressed or deformation experiment was then encapsulated along with zirconia and alumina pistons and spacers inside an iron jacket¹⁵. The aggregate was then hot-pressed at 1,250 °C under a confining pressure of 300 MPa for 3 h in static conditions (no load was applied to the sample). The density of wedge disclinations in this sample is displayed in Extended Data Fig. 1.

EBSD measurements. We analysed the microstructure of four aggregates (OOM, PI-1619, POEM22 and T0548) by EBSD. To ensure high-quality scanning electron microscopy imaging and EBSD analyses, polishing with colloidal silica suspension was necessary after polishing with diamond paste to remove the mechanical damage at the specimen surface. EBSD analyses were conducted with a CamScan X500FE CrystalProbe equipped with an EBSD system³⁰ at Geosciences Montpellier, France. The operating conditions were a voltage of 15 kV, a current of 2.5 nA and a working distance of 20 mm. Low-vacuum conditions (4–5 Pa of gaseous nitrogen) were used to avoid excessive electron charging of sample, in particular grain edges. Data were acquired and treated with CHANNEL5 software.

Several maps were acquired with sampling step sizes of 0.15 μm , 0.2 μm and 0.3 μm (see Extended Data Table 1), which cover up a minimum area of 50 μm

$\times 50 \mu\text{m}$. Raw indexation rates were >83%. Data treatment allowed the rare non-indexed pixels to be filled, if up to six identical neighbours existed with this orientation. A minimum of 3,000 points was always analysed in each map, ensuring a good statistical analysis.

Dislocation and disclination densities measurements. We denote the components of the elastic rotation vector $\vec{\theta}$ as $(\theta_i, i \in (1,2,3))$ along a square grid on the sample surface, aligned with the unit vectors (\vec{e}_1, \vec{e}_2) of the sample reference frame. The disorientation vector between two neighbouring points A and B is $\Delta\theta\vec{r}$, where $\Delta\theta$ denotes the disorientation angle and \vec{r} the disorientation axis. $\Delta\theta\vec{r}$ derives from the rotation mapping one local lattice frame onto the other, or from the disorientation tensor $\overline{\Delta g} = \overline{g_A^{-1}g_B}$ where the orientation tensors $(\overline{g_A}, \overline{g_B})$, specifying the rotation of the lattice at both locations, A and B, are composed. The analysis readily shows that the components $\Delta\theta_i$ of the disorientation vector are¹⁴

$$\Delta\theta_i = \frac{e_{ijk}\Delta g_{jk}\Delta\theta}{2\sin(\Delta\theta)} \quad (5)$$

The grain boundaries and triple junctions were defined as follows from the orientation maps. First, the disorientation of each pixel with its four (north, south, east and west) neighbours was examined. When the disorientation exceeded the ‘grain tolerance angle’ (here 5°), a boundary was defined. Note that, as a consequence, grain boundaries coincide with pixel boundaries. Once the set of all boundaries was captured, a flood-fill procedure was applied to search for sub-areas bounded by a closed boundary. Such sub-areas were defined as grains. A triple junction was acknowledged when three different grains were detected in a 2×2 pixel array.

From the disorientations $\Delta\theta_i$ between neighbouring points separated by Δx_i , only six components of the elastic curvature tensor

$$\kappa_{il}^e = \frac{\Delta\theta_i}{\Delta x_l} \quad (6)$$

can be captured because differences along the normal direction \vec{e}_3 are not available. Using this result, it can be shown from Supplementary equation (28) that five dislocation densities can be recovered in the present reference frame¹⁴, namely $(\alpha_{12}, \alpha_{13}, \alpha_{21}, \alpha_{23}, \alpha_{33})$. The recovery of disclination densities involves the variations in the elastic curvatures. In component form, equation (6) implies

$$\theta_{ij} = e_{jkl}\kappa_{il,k}^e \quad (7)$$

Hence, it is readily seen from equation (7) that the three components $(\theta_{i3}, i \in (1,2,3))$ are directly obtained from conventional planar measurements. In contrast to the recovery of dislocation densities, no additional information about the elastic strain field is needed in this determination. A complete recovery of the nine disclination densities can follow if the variations of curvatures in the third direction \vec{e}_3 become available.

At the present state of the art, the angular accuracy of orientation mapping by EBSD is about 0.5°. In the experiments reported here, the spatial resolution was 0.2 μm , and the spatial accuracy was about 1 nm. In such conditions, equation (7) shows that the disclination densities at grain boundaries are inferred with a 10% error for 5° disorientations, but that the relative error may reduce to about 1% when the disorientation reaches the highest angles, that is, 90° in orthorhombic materials. Therefore, confidence in the results acquired for low-angle boundaries is limited, but the orientation properties of high-angle boundaries should be properly rendered. The five available components of the dislocation density tensor were acquired by using the analysis detailed in ref. 14. With the angular and spatial resolution indicated above, the relative error in their measurement also ranges from about 1% to 10%.

Bi-dimensional modelling of disclinations and grain boundaries. For completeness, the two-dimensional edge-wedge model^{24,25} used in the present work is briefly recalled. We limit the fields of crystal defects envisioned to uniaxial distributions of wedge disclinations, which is sufficient for the interpretation of symmetric tilt boundaries. Thus, we assume the disclination tensor to be $\vec{\theta} = \theta_{33}\vec{e}_3 \otimes \vec{e}_3$ in the orthonormal reference frame $(\vec{e}_1, \vec{e}_2, \vec{e}_3)$, all other components being zero. The continuity condition $\text{div}\vec{\theta} = 0$ is $\theta_{33,3} = 0$, implying that θ_{33} depends only on the coordinates (x_1, x_2) . In component form, the rotational incompatibility equation reads

$$\theta_{ij} = e_{jkl}\kappa_{il,k}^e = -e_{jkl}\kappa_{il,k}^p \quad (8)$$

In the present context, this equation reduces to

$$\theta_{33} = \kappa_{31,2}^p - \kappa_{32,1}^p = \kappa_{32,1}^e - \kappa_{31,2}^e \quad (9)$$

Hence, the only relevant elastic and plastic curvatures are $(\kappa_{31}^e, \kappa_{32}^e)$ and $(\kappa_{31}^p, \kappa_{32}^p)$. Additionally, we note that $\text{Tr}(\overline{\kappa^p}) = 0$. Thus, the disclination transport equation, Supplementary equation (35), is

$$\dot{\theta}_{33} = \dot{\kappa}_{31,2}^p - \dot{\kappa}_{32,1}^p \quad (10)$$

The plastic curvature rate $\overline{\dot{\kappa}}_p$ reads, in component form, $\dot{\kappa}_{ij}^p = e_{jkl} \theta_{ik} V_l^0$, where V_l^0 denotes the l th component of the disclination velocity vector. Hence, we find

$$\begin{aligned}\dot{\kappa}_{31}^p &= -\theta_{33} V_2^0 \\ \dot{\kappa}_{32}^p &= +\theta_{33} V_1^0\end{aligned}\quad (11)$$

Because the trace of the plastic curvature rate tensor vanishes, the source term $\overline{\dot{\kappa}}_p$ in the dislocation transport equation, Supplementary equation (36), feeds only the edge dislocation densities (α_{13}, α_{23}). Using Supplementary equation (34), we can see that the motion of these dislocations produces the plastic strain rate components ($\dot{\epsilon}_{11}^p, \dot{\epsilon}_{12}^p, \dot{\epsilon}_{21}^p, \dot{\epsilon}_{22}^p$):

$$\begin{aligned}\dot{\epsilon}_{11}^p &= -\alpha_{13} V_2^z \\ \dot{\epsilon}_{12}^p = \dot{\epsilon}_{21}^p &= \frac{1}{2}(\alpha_{13} V_1^z - \alpha_{23} V_2^z) \\ \dot{\epsilon}_{22}^p &= \alpha_{23} V_1^z\end{aligned}\quad (12)$$

where V_i^z represent the components of the dislocation velocity vector. The above relations indicate that out-of-plane motion of the edge dislocations (α_{13}, α_{23}) is involved in the extension rates ($\dot{\epsilon}_{11}^p, \dot{\epsilon}_{22}^p$), whereas their glide is responsible for $\dot{\epsilon}_{12}^p$. Consistently, the dislocation transport equation reduces to

$$\begin{aligned}\dot{\alpha}_{13} &= \dot{\epsilon}_{11,2}^p - \dot{\epsilon}_{12,1}^p + \dot{\kappa}_{31}^p \\ \dot{\alpha}_{23} &= \dot{\epsilon}_{21,2}^p - \dot{\epsilon}_{22,1}^p + \dot{\kappa}_{32}^p\end{aligned}\quad (13)$$

Thus, if all other dislocation densities are initially absent, the dislocation distribution involves only edge densities. The Peach–Koehler relationship provides the dislocation velocities in terms of the stress tensor, for both the out-of-plane motion of dislocations (for example, climb or diffusion)

$$\begin{aligned}V_1^z &= +\frac{1}{B_x} \sigma_{22} \alpha_{23} \\ V_2^z &= -\frac{1}{B_x} \sigma_{11} \alpha_{13}\end{aligned}\quad (14)$$

and their glide

$$\begin{aligned}V_1^x &= +\frac{1}{2B_x} (\sigma_{12} + \sigma_{21}) \alpha_{13} \\ V_2^x &= -\frac{1}{2B_x} (\sigma_{12} + \sigma_{21}) \alpha_{23}\end{aligned}\quad (15)$$

Similarly, the constitutive relationships providing the disclination velocities as a function of the couple stresses are²⁴

$$\begin{aligned}V_1^0 &= +\frac{1}{B_x} M_{32} \theta_{33} \\ V_2^0 &= -\frac{1}{B_x} M_{31} \theta_{33}\end{aligned}\quad (16)$$

From the above, it can be seen that the only stress and couple-stress components relevant to the present problem are ($\sigma_{11}, \sigma_{12}, \sigma_{21}, \sigma_{22}$) (where usually $\sigma_{12} \neq \sigma_{21}$, that is, the stress tensor is generally non-symmetric) and (M_{31}, M_{32}), respectively. Hence the Cosserat balance of momentum and moment of momentum equations reduce to

$$\begin{aligned}\sigma_{11,1} + \sigma_{12,2} &= 0 \\ \sigma_{21,1} + \sigma_{22,2} &= 0 \\ M_{31,1} + M_{32,2} + \sigma_{21} - \sigma_{12} &= 0\end{aligned}\quad (17)$$

By taking the curl of equation (17-3) and eliminating the skew-symmetric part of the stress tensor from equation (17-1,2) and the latter, we can rewrite the above system (17) as the higher-order equilibrium equations^{25,31}

$$\begin{aligned}\sigma_{11,1}^{\text{sym}} + \sigma_{12,2}^{\text{sym}} + \frac{1}{2}(M_{31,1}^{\text{dev}} + M_{32,2}^{\text{dev}})_{,2} &= 0 \\ \sigma_{21,1}^{\text{sym}} + \sigma_{22,2}^{\text{sym}} - \frac{1}{2}(M_{31,1}^{\text{dev}} + M_{32,2}^{\text{dev}})_{,1} &= 0\end{aligned}\quad (18)$$

where $\overline{M}^{\text{dev}}$ is the deviatoric part of the couple-stress tensor.

Constitutive elastic laws including non-locality in the core of defects. In the following, constitutive elastic laws for stresses and couple stresses are derived, taking particular account of the nonlocal character of the elastic behaviour, with respect to the crystal symmetry breaking due to crystal defects. In our bi-dimensional model, the Frank vector resulting from the distribution of a wedge disclination density θ_{33} over a surface S in the plane (e_1, e_2) is³²

$$\overline{\Omega} = \int_S \overline{\theta} \cdot \overline{e}_3 dS = \Omega_3 \overline{e}_3 = \int_S \theta_{33} dS \overline{e}_3 \quad (19)$$

In the absence of dislocations, the Burgers vector representing the discontinuity in displacement arising from this rotational incompatibility is³²

$$\overline{b} = - \int_S (\overline{\theta} \times \overline{r}) \cdot \overline{e}_3 dS = - \int_S \theta_{33} x_2 dS \overline{e}_1 + \int_S \theta_{33} x_1 dS \overline{e}_2 = b_1 \overline{e}_1 + b_2 \overline{e}_2 \quad (20)$$

where $\overline{r} = x_1 \overline{e}_1 + x_2 \overline{e}_2$ is the in-plane position vector. We note that the ratio b/Ω of the moduli of the Burgers and Frank vectors

$$b/\Omega = \frac{\left| \int_S (\overline{\theta} \times \overline{r})^t \overline{e}_3 dS \right|}{\left| \int_S \overline{\theta} \cdot \overline{e}_3 dS \right|} \quad (21)$$

defines a length scale characterizing the extent of the defect-containing area. If the disclination density is evenly distributed over the surface S , b/Ω is simply

$$b/\Omega = \frac{1}{S} \int_S r dS \quad (22)$$

Following recent developments³³, we chose the elastic constitutive relations for the symmetric stress tensor $\overline{\sigma}^{\text{sym}}$ and deviatoric couple-stress tensor $\overline{M}^{\text{dev}}$ in the linear form

$$\begin{aligned}\overline{\sigma}^{\text{sym}} &= \overline{C} : \overline{\epsilon}_c + \overline{D} : \overline{\kappa}_c \\ \overline{M}^{\text{dev}} &= \overline{A} : \overline{\kappa}_c + \overline{B} : \overline{\epsilon}_c\end{aligned}\quad (23)$$

The dimensions of the elastic constants in the fourth-order tensors are that of stress (\overline{C}), stress \times length ($\overline{B}, \overline{D}$) and stress \times length² (\overline{A}). Owing to tensor \overline{D} , the inhomogeneity in rotation over the core region induces stresses, whereas the tensor \overline{B} gives rise to couple stresses deriving from the inhomogeneity in strain in this region. Hence, \overline{B} and \overline{D} characterize nonlocal elastic behaviour in the defective crystal. In an isotropic centro-symmetric medium, both \overline{B} and \overline{D} are zero. However, centro-symmetry is broken in the presence of crystal defects, which yields non-zero \overline{B} and \overline{D} tensors³³. Similarly, the elastic tensor \overline{A} induces couple stresses in the defective regions of the crystals, because the symmetry of the stress tensor is broken by the fluctuations of the atomic interactions. Hence, a central issue in the elasticity at the nanometre scale of defect-containing solids consists in relating the tensors of elastic constants ($\overline{A}, \overline{B}$) and \overline{D} to some characteristic length scale pertaining to the defect-containing area, such as the ratio of the Burgers to Frank vector magnitudes introduced above. In the present ‘edge-wedge’ problem, this length scale is found by analysing the inhomogeneity of lattice curvatures and strains in the defect-containing areas. The infinitesimal displacement $d\overline{u} = (\overline{\kappa}_c^e \times \overline{r})^t d\overline{r}$ arising from the inhomogeneity of the lattice curvatures ($\kappa_{31}^e, \kappa_{32}^e$) over the vector $\overline{r} = x_1 \overline{e}_1 + x_2 \overline{e}_2$ in the defect-containing area is, in component form

$$\begin{aligned}du_1 &= -\kappa_{31}^e x_2 dx_1 - \kappa_{32}^e x_2 dx_2 \\ du_2 &= +\kappa_{31}^e x_1 dx_1 + \kappa_{32}^e x_1 dx_2\end{aligned}\quad (24)$$

Hence, we see, for example from equation (24-1) that the curvature κ_{31}^e contributes to a strain ϵ_{11}^e and κ_{32}^e contributes to a strain ϵ_{12}^e . Collecting all such terms, we assume equation (23-1) to be

$$\begin{aligned}\sigma_{11}^{\text{sym}} &= C_{1111} \epsilon_{11}^e + C_{1122} \epsilon_{22}^e - D_{1131} \kappa_{31}^e \\ \sigma_{12}^{\text{sym}} &= C_{1212} \epsilon_{12}^e + C_{1221} \epsilon_{21}^e + D_{1231} \kappa_{31}^e - D_{1232} \kappa_{32}^e \\ \sigma_{21}^{\text{sym}} &= C_{2112} \epsilon_{12}^e + C_{2121} \epsilon_{21}^e + D_{2131} \kappa_{31}^e - D_{2132} \kappa_{32}^e \\ \sigma_{22}^{\text{sym}} &= C_{2211} \epsilon_{11}^e + C_{2222} \epsilon_{22}^e + D_{2231} \kappa_{31}^e\end{aligned}\quad (25)$$

Conversely, in equation (23-2), the infinitesimal rotation $d\overline{r} = \frac{1}{r^2} \overline{r} \times \overline{\epsilon}_c \cdot d\overline{r}$ induced by the inhomogeneity of the in-plane strains ($\epsilon_{11}^e, \epsilon_{12}^e, \epsilon_{22}^e$) over vector $\overline{r} = x_1 \overline{e}_1 + x_2 \overline{e}_2$ produces the curvature components ($\kappa'_{31}, \kappa'_{32}$) such that

$$d\Omega_3 = \frac{1}{r^2} (x_1 \epsilon_{21}^e - x_2 \epsilon_{11}^e) dx_1 + \frac{1}{r^2} (x_1 \epsilon_{22}^e - x_2 \epsilon_{12}^e) dx_2 = \kappa'_{31} dx_1 + \kappa'_{32} dx_2 \quad (26)$$

where $r = \sqrt{x_1^2 + x_2^2}$, which gives rise in turn to the couple-stress components. We therefore conjecture the following relationship between the couple stresses and elastic curvatures and strains:

$$\begin{aligned} M_{31} &= A_{3131} \kappa_{31}^e - B_{3111} \varepsilon_{11}^e + B_{3112} \varepsilon_{12}^e + B_{3121} \varepsilon_{21}^e \\ M_{32} &= A_{3232} \kappa_{32}^e - B_{3211} \varepsilon_{12}^e + B_{3221} \varepsilon_{21}^e + B_{3222} \varepsilon_{22}^e \end{aligned} \quad (27)$$

From the results of ref. 33, the symmetry $B_{ijkl} = D_{ijkl}$ of the elasticities must hold. Thus, for example, $B_{3111} = D_{1131}$, which implies at each point in the defective region, there exist constants (B'_{3111}, D'_{1131}) such that $D'_{1131} x_2 = B'_{3111} x_2 / r^2$ according to equations (24-1) and (26), a relation where the dimension of D'_{1131} is that of a stress and the dimension of B'_{3111} is that of stress \times length squared. Therefore, we may write $B'_{3111} / D'_{1131} = r^2$. The same value r^2 is obtained for all B'_{ijkl} / D'_{ijkl} ratios. r is a characteristic length scale that sets the dimensions of the area over which inhomogeneity of the elastic strains induces a significant couple-stress component. Adopting the above ratio of the Burgers to Frank vector magnitudes, it is given the value $r = 1 \text{ \AA}$ to limit this area to the core region of the defects. Hence, the non-zero components of the elasticity tensors $\left(\begin{smallmatrix} \overline{\overline{\overline{A}}} \\ \overline{\overline{\overline{B}}} \end{smallmatrix}\right)$ and $\overline{\overline{\overline{D}}}$ are simply taken as

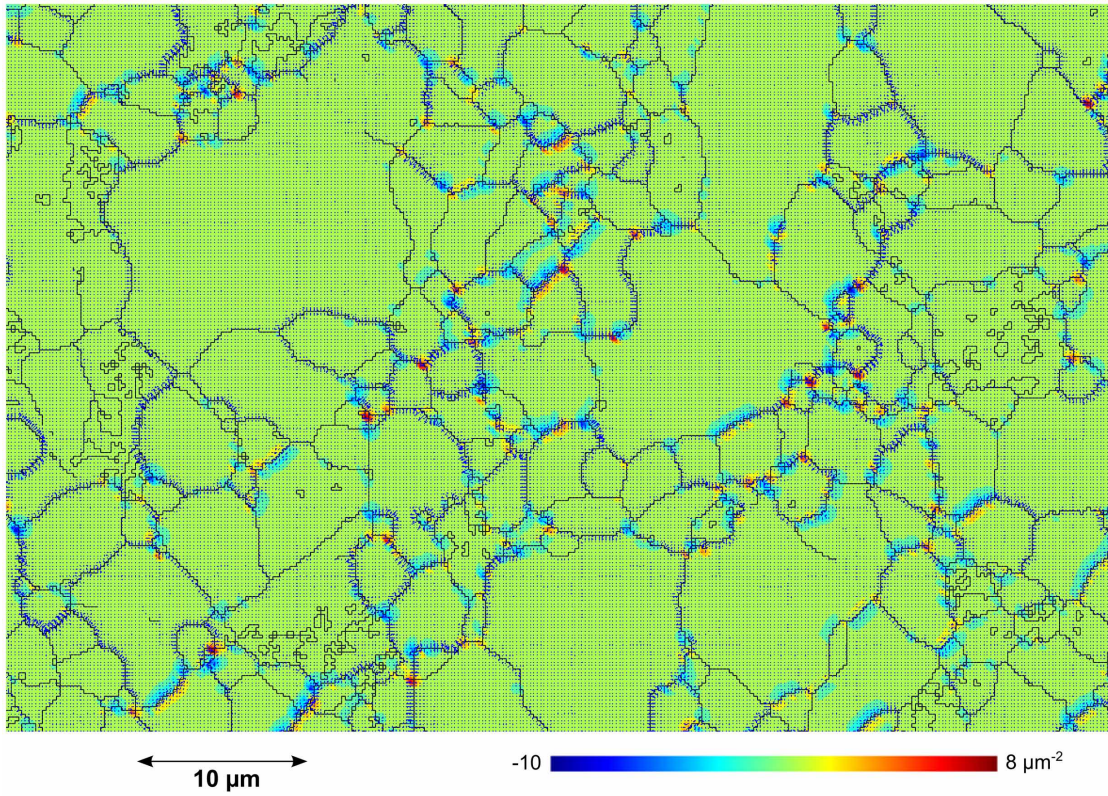
$A_{ijkl} = \mu r^2$, $B_{ijkl} = D_{klij} = \mu r$. In the following simulations, plane strains are assumed in the (100) plane of the olivine unit cell. Elastic coefficients are taken to be³⁴ $C_{1111} = 320.2 \text{ GPa}$, $C_{2222} = 195.9 \text{ GPa}$, $C_{3333} = 233.8 \text{ GPa}$, $C_{2323} = 63.5 \text{ GPa}$, $C_{1313} = 76.9 \text{ GPa}$, $C_{1212} = 78.1 \text{ GPa}$, $C_{1122} = 67.9 \text{ GPa}$, $C_{1133} = 70.5 \text{ GPa}$ and $C_{2233} = 78.5 \text{ GPa}$.

Crossover from atomic to continuous representation of tilt boundaries. The method for constructing a continuous model of a symmetric tilt boundary in copper has been described²⁵. By adopting a spatial resolution (mesh size) below interatomic distances, the atomic structural units that compose the tilt boundary can be conveniently described by wedge disclination dipoles. The arm length t of the dipoles is that of the structural units, while their strength Ω (Frank vector) is related to the Burgers vector b associated with the units, such that $b = \Omega t$. We choose here to model a (011)/[100] tilt boundary of misorientation 60° in olivine, which was simulated earlier using molecular dynamics techniques²¹. As shown in Fig. 4a, the atomic structural units (dashed triangles) exhibit a zigzag configuration in the (100) plane. The Burgers vector associated with these units was estimated to be $b = [001] = 6 \text{ \AA}$, which is the lattice constant c of the olivine unit cell. The [010] direction does not support any component of this Burgers vector. The arm length of the units being the order of 5 \AA , the magnitude of the Frank vector is found to be approximately $\Omega = 1.2 \text{ rad} = 68^\circ$. This magnitude is used to set up the wedge disclination densities through equation (19). The resulting field, shown in Fig. 5 for an element size of approximately 0.05 nm , is used in the

following as the initial disclination field in relaxation simulations, where the disclinations are allowed to move in their own stress and couple-stress fields until the overall elastic energy stabilizes. Periodic boundary conditions are used on vertical boundaries. In this zigzag configuration, the alternative location of the positive/negative disclinations shown in Fig. 4 was preferred to all others because it allows consecutive disclination dipoles to form quadrupoles, which contribute further to energy self-screening. Indeed, we checked that all other configurations lead to a higher elastic energy.

Shear-coupled boundary migration. In the present context of shear-coupled boundary migration, a fundamental consequence of non-local elasticity, defined in equations (25) and (27), is that elastic shear strains generate couple stresses in the defective areas, which sets disclinations into motion according to equations (16). Disclination motion implies motion of the associated dislocation density, which in turn produces plastic shear, even if no dislocation was available beforehand. More precisely, the mechanism is as follows: the non-zero elastic constant B_{3112} induces the couple stress M_{31} under the shear strain ε_{12}^e , which leads to motion normal to the grain boundary of the θ_{33} wedge disclination dipoles (see equation (16-2)). As a result of this disclination dipole motion (which implies normal migration of the grain boundary), the associated edge dislocation density (of [001] character) moves in the defective area along the grain boundary until it annihilates. In the process, plastic shear strain is produced, although no individual perfect dislocation can be identified.

27. Demouchy, S. Diffusion of hydrogen in olivine grain boundaries and implications for the survival of water-rich zones in Earth's mantle. *Earth Planet. Sci. Lett.* **295**, 305–313 (2010).
28. Demouchy, S., Tommasi, A., Boffa Ballaran, T. & Cordier, P. Weak stresses for Earth's uppermost mantle inferred from tri-axial deformation experiments on dry olivine crystals. *Phys. Earth Planet. Inter.* **220**, 37–49 (2013).
29. Paterson, M. S. & Olgaard, D. L. Rock deformation tests to large shear strains in torsion. *J. Struct. Geol.* **22**, 1341–1358 (2000).
30. Demouchy, S. *et al.* Forsterite to wadsleyite phase transformation under shear stress and consequences for the Earth's mantle transition zone. *Phys. Earth Planet. Inter.* **184**, 91–104 (2011).
31. Mindlin, R. D. & Tiersten, H. F. Effects of couple-stresses in linear elasticity. *Arch. Ration. Mech. Anal.* **11**, 415–448 (1962).
32. de Wit, R. in *Fundamental Aspects of Dislocation Theory* Vol. 1 (ed. Simmons, J. A., de Wit, R. & Bullough, R.) 651–680 (National Bureau of Standards, 1970).
33. Upadhyay, M. V., Capolungo, L., Taupin, V. & Fressengeas, C. Elastic constitutive laws for incompatible crystalline media: the contributions of dislocations, disclinations and G-disclinations. *Phil. Mag.* **93**, 794–832 (2013).
34. Webb, S. L. The elasticity of the upper mantle orthosilicates olivine and garnet to 3GPa. *Phys. Chem. Miner.* **16**, 684–692 (1989).



Extended Data Figure 1 | Density of wedge disclinations θ_{33} in the PI-1619 sintered sample. The density is given in radians per square micrometre. The local Burgers vectors arising from edge dislocations are represented by the blue

arrows: their horizontal and vertical components are, respectively, α_{13} and α_{23} (given per micrometre).

Extended Data Table 1 | Parameters related to the EBSD map recorded in this study

| <i>Sample name</i> | <i>Type of deformation</i> | <i>Mineral Phase(s)</i> | <i>EBSD map resolution</i> | <i>EBSD map size</i> |
|--------------------|---|-------------------------|----------------------------|-----------------------------|
| OOM | Mylonite, Oman Ophiolite | Olivine +Opx+sp | 0.15 μm | 168 x 136 μm |
| Poem 22a | Tri-axial compression | Olivine | 0.2 μm | 152 x 124 μm |
| Poem 22b | Tri-axial compression | Olivine | 0.15 μm | 122 x 100 μm |
| PI-1619 | Static hot-pressed (undeformed sample) | Olivine | 0.2 μm | 169.4 x 137.4 μm |
| T0548b | Torsion | Olivine | 0.3 μm | 193 x 157 μm |
| T0548d | Torsion | Olivine | 0.15 μm | 86 x 65 μm |

opx, orthopyroxene; sp, spinel.